



## Magneto-hybrid nanofluid ( $Al_2O_3 / Cu$ –Oil) flow in a porous square enclosure with Cattaneo-Christov heat flow model-sensitivity analysis

N Vinodhini & V Ramachandra Prasad\*

Department of Mathematics, School of Advances Sciences, Vellore Institute of Technology, Vellore 632 014, Tamil Nadu, India

\*E-mail: rcpmaths@gmail.com

Received 6 January 2023; accepted 28 March 2023

The rheological behaviour of nanofluids is an important specification that has a substantial impact on the system performance. The effect of an inclined magnetic field on mixed convection in a square cavity through a porous medium has been numerically investigated in the current paper. Various levels of thermal conductivity have been maintained on each wall throughout the system. Additionally, the Cattaneo-Christov heat flow model is influenced in the energy equation. The conservation equations for primary, secondary, and mass momentum, energy, and nanoparticles with wall boundary conditions are dimensionless and coupled to proper scaling transformations. To address the dimensionless nonlinear coupled boundary value problem, a finite-difference computing methodology known as the Harlow-Welch Marker and Cell (MAC) method is used. The fundamental goal of this research is to look at the rheological behaviour of nanoparticles as base fluids in the aforementioned effects. The influence of factors on the physical framework such as Richardson number (Ri), Hartmann number (Ha), Darcy number (Da), Reynolds number (Re), and Prandtl number (Pr) is investigated graphically. The MATLAB software is used to obtain streamlined and isothermal contours. The findings indicate an enhancement in the average Nusselt number with an increase in the parameters. Furthermore, the presence of nanoparticles raises the average Nusselt number for low values of the Reynolds number. The system is analyzed with three convection stages of Richardson number, and it is also found that for mixed convection, the system holds better results. The obtained outcomes are compared with well-known existing findings to validate the present work.

**Keywords:** Mixed convection,  $Al_2O_3 / Cu$  –Oil nanoparticles, Porous medium, Inclined magnetic field, Cattaneo-Christov model

Liquid coolant is commonly used to reduce overheating or increase the rate of heat transfer. Several more studies of the thermal physical characteristics of widely accepted liquid coolants that are used as heat transfer fluids indicate that they have lower thermal conductivity when compared with solid metals. Various methods were utilized in the previous period to significantly enhance heat transfer rates. There are several ways to increase the efficiency of heat transfer. One of these methods was to increase the working fluid's thermal conductivity. Common fluids for heat transfer, such as water, engine oil, and ethylene glycol, have low thermal conductivity when compared to solids. To improve the thermal properties of conventional fluids for heat transfer, solid particles with high thermal conductivity were dispersed in the base fluid. Introducing small solid particles into a fluid with high thermal conductivity increases the thermal conductivity of the same fluid. Several researchers have previously investigated the feasibility of using these mixtures of solid particles with sizes ranging from 2 mm to micrometers and

major downsides have been discovered<sup>1</sup>. At Argonne National Laboratory, when Choi and Eastman<sup>2</sup> returned to this area with their suspensions of nanoscale metallic particles and carbon nanotubes, the situation changed.

Numerous investigations have attempted to revoke metal and metal oxide nanoparticles in a variety of fluids<sup>3,4</sup>. Because of rising energy demands, emerging technologies recognize the importance of the recent heat-transferred liquid with superior properties known as "Nanofluid". A nanofluid is one of the appropriate maintenance heat transfer enhancement strategies used in the majority of thermal performance, including solar collectors, heat exchangers, biomedical devices, thermal storage, electronic component cooling, engine/vehicle cooling, and nuclear reactor transformers. The utilization of nanofluids containing multiple nanoparticles provides a significant thermal performance improvement greater than that of each base fluid, estimated based on the particle fraction<sup>5</sup>. Many scientists have used various types of nanoparticles to determine the

coefficient of convective heat transfer flowing nanofluids through a tube, including  $Al_2O_3$ , carbon nanotubes (CNT), CuO, Cu,  $Fe_2O_3$ ,  $Fe_3O_4$ , nanodiamond (ND),  $TiO_2$ ,  $SiO_2$ ), silver, SiC, and zirconia. Hybrid nanoparticles have been utilized to enhance heat transfer in applications by acting as heat exchangers because they have significantly better thermophysical properties than conventional fluids. Several more studies have extensively studied hybrid nanofluid introduction due to increased heat transfer in comparison with nanofluids. In a hybrid nanofluid, two different types of nanoparticles are suspended in a base fluid. The current research focuses on such issues and analyses heat transfer characteristics in square enclosures. Asadi<sup>6</sup> had done an experimental investigation of the CuO- $TiO_2$ /water hybrid nanofluid's portrayal, stability, and dynamic viscosity.

Abu-Nab<sup>7</sup> examines the non-linear multi-bubble framework in Newtonian medium by considering the bubble-bubble (BB) interplay in a Cu- $Al_2O_3/H_2O$  hybrid nanofluid through the radius of the vapour bubble. The transient stagnant flow of the hybrid nanofluid is considered by Khashi *et al.*<sup>8</sup> when thermal radiation is present on an impermeable disk. He assessed the correlations of the existing hybrid nanofluids and numerically applied them to the pair of copper and aluminium oxide with 2%  $\phi_{nmf}$ . He emphasized radiative Cu- $Al_2O_3/H_2O$  hybrid nanofluid flow toward an EMHD plate: shape factor effect. Ammar *et al.*<sup>9</sup> implemented a two-phase hybrid nanofluid on mixed convection to simulate the impact in a wavy lid driven cavity with a localized solid block. In numerous case studies, he employed hybrid  $Al_2O_3$ -Cu/water nanofluids. Christopher *et al.*<sup>9</sup> utilized numerical simulation and series solution to study the effects of Cattaneo-Christov heat flux and homogeneous-heterogeneous reactions on the hybrid nanofluids flow over a stretched cylinder. He used water as the base liquid to dissolve two different nanoparticles,  $Al_2O_3$  and Cu. Zhang *et al.*<sup>10</sup> have studied the outcome of heat transfer in melting a Cattaneo-Christov heat flux rotary flow of gold-silver/engine oil hybrid nanofluid. A hybrid nanofluid containing copper-alumina lodgings in the base liquid water is employed by Khan<sup>11</sup> to present a model for 3D-axis symmetric flows and heat dissipation. Under the influence of hot air and Cattaneo-Christov heat conduction, also known as the (AMH-HNF-TCCHF) flow model, this flow passes over a biaxial porous stretching/lowering sheet. Haddad<sup>12</sup> thought about the

fluid inertia and thermal destabilization in a porous Brinkman medium. Boundaries that are fixed and free are both examined. In the heat flux constitutive equation, he had included the Cattaneo-Christov theory. Three oxide-based nanofluids ( $Al_2O_3 - TiO_2 - SiO_2$ ) were evaluated numerically, and their hybrids are suggested by Adriana<sup>13</sup>. Usman *et al.*<sup>14</sup> explore the important effects of thermal conductivity with time dependence and nonlinear thermal radiation caused by rotating Cu- $Al_2O_3$  -water hybrid nanofluid flow over a 3D stretching sheet. Siddiqui *et al.*<sup>15</sup> describe the trade-off between Cu- $Al_2O_3$  hybrid nanofluid scatter stability and heat transport for various mixing ratios. Saeed<sup>16</sup> describes entropy generation and natural convective heat transfer of an  $Al_2O_3$ /water nanofluid with an elliptic constant temperature in a tilted enclosure as follows: Making use of magnetic fields and radiation effects. The effect of water-based  $Al_2O_3$  and  $Al_2O_3$ -Cu hybrid nanofluids on forced convection was numerically analysed by Moghadassi *et al.*<sup>17</sup>. Additionally, the fluid, energetic performance was assessed by the authors. Das<sup>18</sup> defined the entropy generation property of Cu- $Al_2O_3$ /Ethylene Glycol hybrid nanofluids flowing through a rotating channel. Hakim<sup>19</sup> focused on the natural convection of a Cu- $Al_2O_3$  an inclined enclosure with wavy walls containing a hybrid nanofluid. Sui *et al.*<sup>20</sup> presented a thorough analysis of mass transportation and heat in the boundary layer phenomena using Cattaneo-Christov dual dispersion in a top-convection Maxwell nanofluids through a velocity profile stretching sheet.

Gnaneswara *et al.*<sup>21</sup> concentrated on the 2D flows pertaining to an incompressible hybrid dust-liquid along with an elongated sheet via a Darcy Forchheimer channel. The properties of carbon nanotubes and the Cattaneo-Christov heat flow model were considered. Rashmi *et al.*<sup>22</sup> have used the Cattaneo-Christov heat flow model and heat generation. To analyse the hybrid nanofluids in a steady state over two distinct geometries, a prototype with a correlation coefficient and probable error was developed. In the presence of an inclined magnetic field, Elshehabey *et al.*<sup>23</sup> probed the natural convection of nanofluids in an oblique L-shaped cavity in a numerical study containing Cu/water nanofluids. Rui *et al.*<sup>24</sup> looked at how the Lorentz force affected an air circulation enclosure with a heated baffle in the center that was filled with a Cu- $Al_2O_3$ - $H_2O$  hybrid nanofluid. The vertical

heating blocks are placed in the centre of the cavity. Mehryan *et al.*<sup>25</sup> evaluated the natural convection of  $Al_2O_3$ –Cu water nanofluids in a partially porous heated chamber. For the porous matrix, two forms of critical porous media are considered: glass balls and aluminium metal foam. Suresh *et al.*<sup>26</sup> synthesized the  $Al_2O_3$ –Cu/water Nanofluid in 2 phases and studied their thermophysical characteristics. Aladdin *et al.*<sup>27</sup> looked at the flow of a Cu– $Al_2O_3$ /water hybrid nanofluids across a permeability progression system with hydromagnetic and sucking effects. Tahira *et al.*<sup>28</sup> made an effort to ensure that the flows of Cu– $Al_2O_3$ /water hybrid nanofluids over a heating porosity barrier are rotationally symmetrical. Lund *et al.*<sup>29</sup> created hybrid nanoparticles consisting of Cu and  $Al_2O_3$ . He also steps forth to investigate the stability analysis and multiple hybrid nanomaterial solutions are applied to a contracting surface in the presence of viscous dissipation. Hamdeh *et al.*<sup>30</sup> carried out a numerical study on heat exchange from the surface of a solar collector container filled with oil NEPCM/ $Al_2O_3$  in the superconducting state. Khan *et al.*<sup>31</sup> examined the numerical analysis of the Cattaneo-Christov heat flow models for viscous flow caused by a rapidly stretched surface. C.I. Christov<sup>32</sup> noted the Maxwell-Cattaneo finite-speed heat conduction model on a frame-indifferent formulation. Uma Devi and Anjali Devi<sup>33</sup> conducted a numerical study on the 3D hybrid Cu– $Al_2O_3$ /Water nanofluid flow of Lorentz force acting on a stretched sheet influencing Newtonian heat transfer. Their investigation showed the heat transmission rate of hybrid nanofluids (Cu– $Al_2O_3$ /Water) was greater than that of nanofluids (Cu/Water) in the magnetic field that was applied. Meena and Pranitha<sup>34</sup> investigated the effect of double dispersion saturated non-Darcy porous media on power-law nanofluids in mixed convection. Pranitha and Meena<sup>35</sup> looked at the Soret and Dufour effects on a vertical cone saturated porous medium to see how double dispersion affected natural convection flow. Meena *et al.*<sup>36</sup> investigated the mixed convection flow over a vertically cone saturated porous medium with a double dispersion effect. O.P. Meena<sup>37</sup> analyzed mixed convection fluid flow over a vertical cone-saturated porous medium with double dispersion and injection/suction effects.

The aforementioned literature survey exposes that the present work has no impact previously achieved using the same combination. An interest in numerically exploring hybrid nanofluidic flows

through the Cattaneo-Christov heat flow model. The impact of Cattaneo-Christov heat flow model on the mixed convection flow over a porous medium in an incompressible fluid with a combination of two nanoparticles is taken into consideration. We aimed to examine it in this piece of contribution, which became essential after a deep literature survey. In the proposed investigation, an extensive mathematical model is created to probe the thermal performance effectiveness of  $Al_2O_3$ –Cu–Oil hybrid nanofluid through an enclosure having a square-shaped geometry. The furnished work has the cold slits placed at the top and centre of the right wall, while the hot slits at the bottom and centre of the left wall employ an inclined magneto-hydrodynamic effect. The system is influenced by a porous medium. A powerful nonlinear system governing structure is computed numerically using suitable similarity modifications. The technique encountered in the present study is the MAC scheme<sup>38,3</sup>. The graphic results are explained to depict the characteristics of  $Al_2O_3$ /Cu–Oil nanofluid transport processes utilizing streamlines, isotherms, and local Nusselt number distributions. The response surface methodology study is analysed and the residual plots are also pictured in the results and discussion section, which helps to obtain the optimal state of the parameters that impact the present findings most.

## Mathematical Formulation

### The problem configuration

The problem flow is laminar, time-varying, and an incompressible mixed convection flow over a porous medium proposing 2D flow in a square shaped enclosure. The medium is filled with hybrid nanofluids, which comprise nanoparticles  $Al_2O_3$ –Cu and oil as the base fluid. Fig. 1 shows the physical description of the system. Let “L” denote the length of the square cavity. The hot slits are located in the horizontal base and center of the vertical left wall, while the cold slits are placed at the top and center of the right vertical wall. Gravitational acceleration has an effect on the vertically descending surface. The magnetic field of force  $B_0$  with inclination is influenced in the horizontal direction. The thermo-physical characteristics of the base fluids and different nanoparticles are given in Table 1. The system is equipped with the Cattaneo-Christov heat flow model<sup>40</sup>.

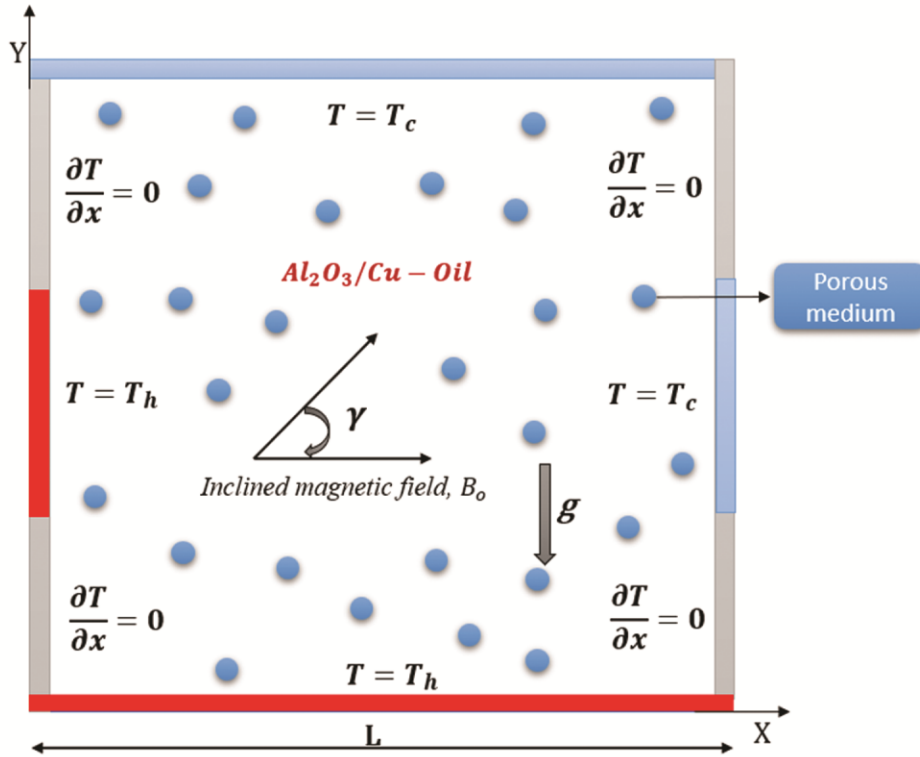


Fig. 1 — Schematic representation of the system

Table 1 — Thermophysical properties of oil and nanoparticles<sup>44-45</sup>

Property	Oil	$Al_2O_3$	Cu
$\rho(kgm^{-3})$	640	3970	8,933
$C_p(Jkg^{-1}K^{-1})$	2132	765	385
$k(Wm^{-1}k^{-1})$	0.0733	40	401
$\beta(k^{-1})$	$64 \times 10^{-5}$	$0.85 \times 10^{-5}$	$1.67 \times 10^{-5}$
$\sigma(\Omega^{-1}m^{-1})$	$2 \times 10^{-4}$	$1 \times 10^{-10}$	$5.96 \times 10^7$
$Pr$	4.62	-	-

**The governing equations**

The major equations that govern fluid behaviour are presented in the following<sup>41,42</sup>:

$$\frac{\partial u}{\partial x} + \frac{\partial v}{\partial y} = 0 \quad \dots (1)$$

$$\frac{\partial u}{\partial t^*} + u \frac{\partial u}{\partial x} + v \frac{\partial u}{\partial y} = -\frac{1}{\rho_{hnf}} \frac{\partial p}{\partial x} + v_{hnf} \left[ \frac{\partial^2 u}{\partial x^2} + \frac{\partial^2 u}{\partial y^2} \right] -$$

$$\frac{v_{hnf}}{K} u + \frac{(\rho\beta)_{hnf}}{\rho_{hnf}} g(T - T_c) \sin(\gamma) \quad \dots (2)$$

$$\frac{\partial v}{\partial t^*} + u \frac{\partial v}{\partial x} + v \frac{\partial v}{\partial y} = -\frac{1}{\rho_{hnf}} \frac{\partial p}{\partial y} + v_{hnf} \left[ \frac{\partial^2 v}{\partial x^2} + \frac{\partial^2 v}{\partial y^2} \right]$$

$$-\frac{v_{hnf}}{K} v + \frac{(\rho\beta)_{hnf}}{\rho_{hnf}} g(T - T_c) \cos(\gamma)$$

$$-\frac{\sigma_{hnf} B_0^2}{\rho_{hnf}} v \quad \dots (3)$$

$$\frac{\partial T}{\partial t^*} + u \frac{\partial T}{\partial x} + v \frac{\partial T}{\partial y} = \alpha_{hnf} \left[ \frac{\partial^2 T}{\partial x^2} + \frac{\partial^2 T}{\partial y^2} \right]$$

Table 2 — Dimensionless requirements

Heat flux	$Q$	$\frac{Q_0 L^2}{(\rho C_p)_{bf} \alpha_{bf}}$
Prandtl number	$Pr$	$\frac{\nu_f}{\alpha_f}$
Reynolds number	$Re$	$\frac{U_0 L}{\nu_f}$
Grashof number	$Gr$	$\frac{g \beta_f (T_h - T_c) L^3}{\nu_f^2}$
Hartmann number	$Ha$	$B_0 L \sqrt{\frac{\sigma_{bf}}{\mu_{bf}}}$
Darcy parameter	$Da$	$\frac{K}{L^2}$
Richardson number	$Ri$	$\frac{Gr}{Re^2}$
Cattaneo Christov heat flux parameter	$\Upsilon_e$	$\frac{\Upsilon U_0}{L}$

$$-\gamma \left( \begin{array}{l} u \frac{\partial u}{\partial x} \frac{\partial T}{\partial x} + v \frac{\partial v}{\partial y} \frac{\partial T}{\partial y} + u^2 \frac{\partial^2 T}{\partial x^2} + v^2 \frac{\partial^2 T}{\partial y^2} + \\ 2uv \frac{\partial^2 T}{\partial x \partial y} + u \frac{\partial v}{\partial x} \frac{\partial T}{\partial y} + v \frac{\partial u}{\partial y} \frac{\partial T}{\partial x} \end{array} \right) \dots (4)$$

Velocity components are denoted by  $u$  and  $v$  in the  $x$  and  $y$  directions, respectively, the temperature of the fluid is  $T$ , time variant of the fluid is  $t$ , and the pressure of the fluid is  $p$ . Accordingly,  $(\rho\beta)_{hnf}$ ,  $\mu_{hnf}$ ,  $\alpha_{hnf}$ ,  $\rho_{hnf}$ ,  $\sigma_{hnf}$ ,  $(\rho C_p)_{hnf}$  these represents thermal expansion, dynamic viscosity, thermal diffusivity, density electrical conductivity, and heat capacitance of the fluid. Table 2 represents the dimensionless parameters of the present problem.

**The boundary conditions**

The enforced boundary conditions of the flow are listed as follows:

Left wall	$x = 0, 0 < y < L, u = v = 0$	$\frac{\partial T}{\partial x} = 0, for 0 < y < \frac{L}{4}$ $T = T_h, for \frac{L}{4} < y < \frac{3L}{4}$ $\frac{\partial T}{\partial x} = 0, for \frac{3L}{4} < y < L$
Right wall	$x = L, 0 < y < L, u = v = 0$	$\frac{\partial T}{\partial x} = 0, for 0 < y < \frac{L}{4}$ $T = T_c, for \frac{L}{4} < y < \frac{3L}{4}$ $\frac{\partial T}{\partial x} = 0, for \frac{3L}{4} < y < L$

Bottom wall  $y = 0, 0 < x < L, u = v = 0$   $T = T_h, for 0 < x < L$   
 Top wall  $y = L, 0 < x < L, u = v = 0$   $T = T_c, for 0 < x < L$

... (5)

**Thermophysical properties of hybrid nanofluids<sup>43</sup>**

**Density**

$\rho_{hnf} = (1 - \varphi)\rho_{bf} + \varphi_{Al_2O_3}\rho_{Al_2O_3} + \varphi_{cu}\rho_{cu}$  ... (6)

**Heat Capacitance**

$(\rho C_p)_{hnf} = (1 - \varphi)(\rho C_p)_{bf} + \varphi_{Al_2O_3}(\rho C_p)_{Al_2O_3} + \varphi_{cu}(\rho C_p)_{cu}$  ... (7)

**Thermal expansion co-efficient**

$\alpha_{hnf} = \frac{k_{hnf}}{(\rho C_p)_{hnf}}$  ... (8)

**Electrical conductivity**

$\frac{\sigma_{hnf}}{\sigma_{bf}} = 1 + \frac{3 \left( \frac{(\varphi_{Al_2O_3} \sigma_{Al_2O_3} + \varphi_{cu} \sigma_{cu})}{\sigma_{bf}} (\varphi_{Al_2O_3} + \varphi_{cu}) \right)}{\left( \frac{(\varphi_{Al_2O_3} \sigma_{Al_2O_3} + \varphi_{cu} \sigma_{cu})}{\sigma_{bf}} + 2 \right) - \left( \frac{(\varphi_{Al_2O_3} \sigma_{Al_2O_3} + \varphi_{cu} \sigma_{cu})}{\sigma_{bf}} (\varphi_{Al_2O_3} + \varphi_{cu}) \right)}$  ... (9)

**Effective**

**viscosity** =  $\frac{\mu_{bf}}{(1 - \varphi_{Al_2O_3})^{2.5} (1 - \varphi_{cu})^{2.5}}$  ... (10)

**Effective Thermal conductivity**

$\frac{k_{hnf}}{k_{bf}} = \left( \frac{(\varphi_{Al_2O_3} k_{Al_2O_3} + \varphi_{cu} k_{cu})}{\varphi} + 2k_{bf} \right) 2\varphi k_{bf} \times -1$   
 $\left( \frac{(\varphi_{Al_2O_3} k_{Al_2O_3} + \varphi_{cu} k_{cu})}{\varphi} + 2k_{bf} - (\varphi_{Al_2O_3} k_{Al_2O_3} + \varphi_{cu} k_{cu}) + \varphi k_{bf} \right)$  ... (11)

The foregoing is some non - dimensional entities:

$X = \frac{x}{L'} = \frac{y}{L}; U = \frac{u}{U_0}; V = \frac{v}{U_0}; t = \frac{t^* U_0}{L}; P = \frac{p}{\rho_f U_0^2}; \theta = \frac{T - T_c}{T_h - T_c}$  ... (12)

The non-dimensional version of the partial differential Eqs.(PDE) (1) - (4) is illustrated below:

$\frac{\partial U}{\partial X} + \frac{\partial V}{\partial X} = 0$  ... (13)

$$\frac{\partial U}{\partial t} + U \frac{\partial U}{\partial X} + V \frac{\partial U}{\partial Y} = - \left( \frac{\rho_f}{\rho_{hnf}} \right) \frac{\partial P}{\partial X} + \left( \frac{v_{hnf}}{v_f} \right) \frac{1}{Re} \left[ \frac{\partial^2 U}{\partial X^2} + \frac{\partial^2 U}{\partial Y^2} \right] - \left( \frac{v_{hnf}}{v_f} \right) \frac{U}{ReDa} + \frac{\beta_{hnf}}{\beta_f} Ri\theta \sin(\gamma) \quad \dots (14)$$

$$\frac{\partial V}{\partial t} + U \frac{\partial V}{\partial X} + V \frac{\partial V}{\partial Y} = - \left( \frac{\rho_f}{\rho_{hnf}} \right) \frac{\partial P}{\partial Y} + \left( \frac{v_{hnf}}{v_f} \right) \frac{1}{Re} \left[ \frac{\partial^2 V}{\partial X^2} + \frac{\partial^2 V}{\partial Y^2} \right] - \left( \frac{v_{hnf}}{v_f} \right) \frac{V}{ReDa} + \frac{\beta_{hnf}}{\beta_f} Ri\theta \cos(\gamma) - \left( \frac{\rho_f}{\rho_{hnf}} \right) \left( \frac{\sigma_{hnf}}{\sigma_f} \right) \frac{Ha^2}{Re} V \quad \dots (15)$$

$$\frac{\partial \theta}{\partial t} + U \frac{\partial \theta}{\partial X} + V \frac{\partial \theta}{\partial Y} = \left( \frac{\alpha_{hnf}}{\alpha_f} \right) \frac{1}{RePr} \left[ \frac{\partial^2 \theta}{\partial X^2} + \frac{\partial^2 \theta}{\partial Y^2} \right] - \gamma_e \left( U \frac{\partial U}{\partial X} \frac{\partial \theta}{\partial X} + V \frac{\partial V}{\partial Y} \frac{\partial \theta}{\partial Y} + U^2 \frac{\partial^2 \theta}{\partial X^2} + V^2 \frac{\partial^2 \theta}{\partial Y^2} + 2UV \frac{\partial^2 \theta}{\partial X \partial Y} + U \frac{\partial V}{\partial X} \frac{\partial \theta}{\partial Y} + V \frac{\partial U}{\partial Y} \frac{\partial \theta}{\partial X} \right) \quad \dots (16)$$

Non – dimensional boundary conditions are:

Left wall	$X = 0, 0 < Y < 1, U = V = 0$	$\frac{\partial \theta}{\partial X} = 0, for 0 < Y < \frac{1}{4}$ $\theta = 1, for \frac{1}{4} < Y < \frac{3}{4}$ $\frac{\partial \theta}{\partial X} = 0, for \frac{3}{4} < Y < 1$
Right wall	$X = 1, 0 < Y < 1, U = V = 0$	$\frac{\partial \theta}{\partial X} = 0, for 0 < Y < \frac{1}{4}$ $\theta = 0, for \frac{1}{4} < Y < \frac{3}{4}$ $\frac{\partial V}{\partial X} = 0, for \frac{3}{4} < Y < 1$
Bottom wall	$Y = 0, 0 < X < 1, U = V = 0$	$\theta = 1, for 0 < X < L$
Top wall	$Y = 1, 0 < X < 1, U = V = 0$	$\theta = 0, for 0 < X < L$

... (17)

**Nusselt number**

The succeeding equation can be used to obtain the local Nusselt number.

$$Nu = - \frac{k_{hnf}}{k_{bf}} \left( \frac{\partial \theta}{\partial Y} \right)_{Y=0} \quad \dots (18)$$

**Numerical MAC method**

The governing equations for non-dimensional systems i.e. Eqs. (13)- (16) have been resolved using a numerical methodology based on the finite difference method. The key difference in both the X and Y axes is that the second derivatives have been estimated using quotients. The Marker and Cell (MAC) method is utilized to analyse the discretized equations that are generated. The parameters U and V indicate the numerical representations of the velocity components. In this article, the Brinkman model<sup>46</sup> is employed to determine the viscosity of the respective hybrid nanofluids. As a preliminary step, the formula calculates the efficient dynamic viscosity of the hybrid nanofluids. Use the following notation to apply a grid meshing method to the center of the cells:

$$U_{i-\frac{1}{2},j} = \frac{1}{2} (U_{i-1,j} + U_{i,j}) \quad \dots (19)$$

The subscriptions i and j designate grid positions among the X and Y axes. Eq. (19) is incorporated with the momentum equation in the x-direction portrayal of the Advent period:

**Advection term discretization**

$$\frac{\partial(UU)}{\partial X} = \frac{UU_1 - UU_2}{\Delta X} \quad \dots (20)$$

$$UU_1 = \left( \frac{1}{2} (U_{i,j} + U_{i+1,j}) \right)^2 \quad \dots (21)$$

$$UU_2 = \left( \frac{1}{2} (U_{i-1,j} + U_{i,j}) \right)^2 \quad \dots (22)$$

Accordingly,

$$\frac{\partial(UV)}{\partial Y} = \frac{UV_1 - UV_2}{\Delta Y} \quad \dots (23)$$

Here,

$$UV_1 = \frac{1}{2} (U_{i,j} + U_{i,j+1}) \cdot \frac{1}{2} (V_{i,j} + V_{i+1,j}) \quad \dots (24)$$

$$UV_2 = \frac{1}{2} (U_{i,j} + U_{i,j-1}) \cdot \frac{1}{2} (V_{i,j-1} + V_{i+1,j-1}) \quad \dots (25)$$

For the second-order differential equation, the preceding central difference formula is used:

$$\nabla^2 U = \frac{\partial^2 U}{\partial X^2} + \frac{\partial^2 U}{\partial Y^2} \quad \dots (26)$$

$$\nabla^2 U = \frac{U_{i-1,j} - 2U_{i,j} + U_{i+1,j}}{\Delta X^2} + \frac{U_{i,j-1} - 2U_{i,j} + U_{i,j+1}}{\Delta Y^2} \quad \dots (27)$$

Replacing Eq. (17) into the y-direction momentum equation Eq. (14) yields:

$$\text{Advection term} \quad \frac{\partial(VU)}{\partial X} = \frac{VU_1 - VU_2}{\Delta X} \quad \dots (28)$$

This method employs the following notations:

$$UV_1 = \frac{1}{2}(U_{i,j+1} + U_{i,j}) \cdot \frac{1}{2}(V_{i,j} + V_{i+1,j}) \quad \dots (29)$$

$$UV_2 = \frac{1}{2}(U_{i-1,j+1} + U_{i-1,j}) \cdot \frac{1}{2}(V_{i,j} + V_{i-1,j}) \quad \dots (30)$$

$$\frac{\partial(VV)}{\partial Y} = \frac{VV_1 - VV_2}{\Delta Y} \quad \dots (31)$$

$$VV_1 = \left(\frac{1}{2}(V_{i,j+1} + V_{i,j})\right)^2 \quad \dots (32)$$

$$VV_2 = \left(\frac{1}{2}(V_{i,j-1} + V_{i,j})\right)^2 \quad \dots (33)$$

The numerical model of the Laplacian operator is given by the central difference.

$$\nabla^2 V = \frac{\partial^2 V}{\partial X^2} + \frac{\partial^2 V}{\partial Y^2} \quad \dots (34)$$

$$\nabla^2 V = \frac{V_{i-1,j} - 2V_{i,j} + V_{i+1,j}}{\Delta X^2} + \frac{V_{i,j-1} - 2V_{i,j} + V_{i,j+1}}{\Delta Y^2} \quad \dots (35)$$

The following is the discretization strategy for the X-momentum equation for the next time level ( $U^{n+1}$ ) is as follows:

$$U^{n+1} = U^n + dt \left\{ -\left( U \frac{\partial U}{\partial X} + V \frac{\partial U}{\partial Y} \right) + \frac{1}{Re} \left( \frac{\partial^2 U}{\partial X^2} + \frac{\partial^2 U}{\partial Y^2} - \frac{1}{Da} U \right) + Ri \theta \sin(\gamma) \right\} \quad \dots (36)$$

The discretization approach for the Y-momentum equation for the next time level ( $V^{n+1}$ ) must be somewhat altered with the inclusion of a new term, and takes the form:

$$V^{n+1} = V^n + dt \left[ -\left( U \frac{\partial V}{\partial X} + V \frac{\partial V}{\partial Y} \right) + \frac{1}{Re} \left( \frac{\partial^2 V}{\partial X^2} + \frac{\partial^2 V}{\partial Y^2} - \frac{1}{Da} V \right) - \frac{Ha^2}{Re} V + Ri \theta \cos(\gamma) \right] \quad \dots (37)$$

Before being employed in the previous equation, the temperature ( $\theta$ ) is co-located with velocity to account for the staggered grid. The Poisson pressure

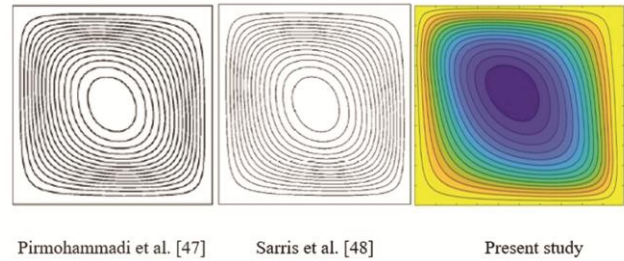


Fig. 2 — Comparison of streamline contours for  $Ha=25$ ;  $Da=0.001$ ;  $Re=2$ ;  $Ri=1$ ;  $\gamma = 30^\circ$ ;  $\gamma_e = 0.02$

equation is used to derive  $U$  and  $V$  after projecting  $U^{n+1}$  and  $V^{n+1}$ .

$$\frac{\nabla^2 U}{dt} = \nabla^2 p \quad \dots (38)$$

For the following time level ( $\theta^{n+1}$ ), the temperature equation can be discretized as follows:

$$\theta^{n+1} = \theta^n + \Delta t \left( -\left( U \frac{\partial \theta}{\partial X} + V \frac{\partial \theta}{\partial Y} \right) + \frac{1}{Re Pr} \left( \frac{\partial^2 \theta}{\partial X^2} + \frac{\partial^2 \theta}{\partial Y^2} \right) + \left( U \frac{\partial U}{\partial X} + V \frac{\partial V}{\partial Y} + U^2 \frac{\partial^2 \theta}{\partial X^2} + V^2 \frac{\partial^2 \theta}{\partial Y^2} + 2UV \frac{\partial^2 \theta}{\partial X \partial Y} + U \frac{\partial V}{\partial X} + V \frac{\partial U}{\partial Y} \right) \right) \quad \dots (39)$$

Fig. 2 shows the comparison results of streamlines for a fixed  $Ha$  value with varying parameters. The accuracy of the findings compared with Pirmohammadi *et al.*<sup>47</sup> and Sarris *et al.*<sup>48</sup> available details illustrated in the figure. The overall comparison result shows a high level of agreement. The present study is validated using the MAC algorithm code, which indicates that the study is more appropriate with the existing results.

## Results and Discussion

In the foregoing work, the numerical MAC method is used to analyse the magnetic hybrid nanofluids in the presence of  $Al_2O_3/Cu - Oil$  in a saturated porous medium with a square cavity influenced by the Cattaneo-Christov heat flow parameter. The effect of heat transmission on various pertinent parameters is discussed in this section. With the exception of differences between the figures, all such values are presumed to remain fixed throughout the computation.  $Pr = 4.62$ ;  $Re = 2$ ;  $Ri = 1$ ;  $Da = 0.001$ ;  $\gamma = 30^\circ$ ;  $\gamma_e = 0.02$ ;  $Ha = 10$  respectively. For different values of the involved parameters, such as Darcy number ( $Da$ ), Hartmann number ( $Ha$ ), Richardson number ( $Ri$ ), Magnetic field inclination ( $\gamma$ ), Reynolds number ( $Re$ ), and Prandtl number ( $Pr$ ). The numerical results obtained are distinguished by typical streamlines, isotherms, local Nusselt numbers, and average Nusselt numbers.

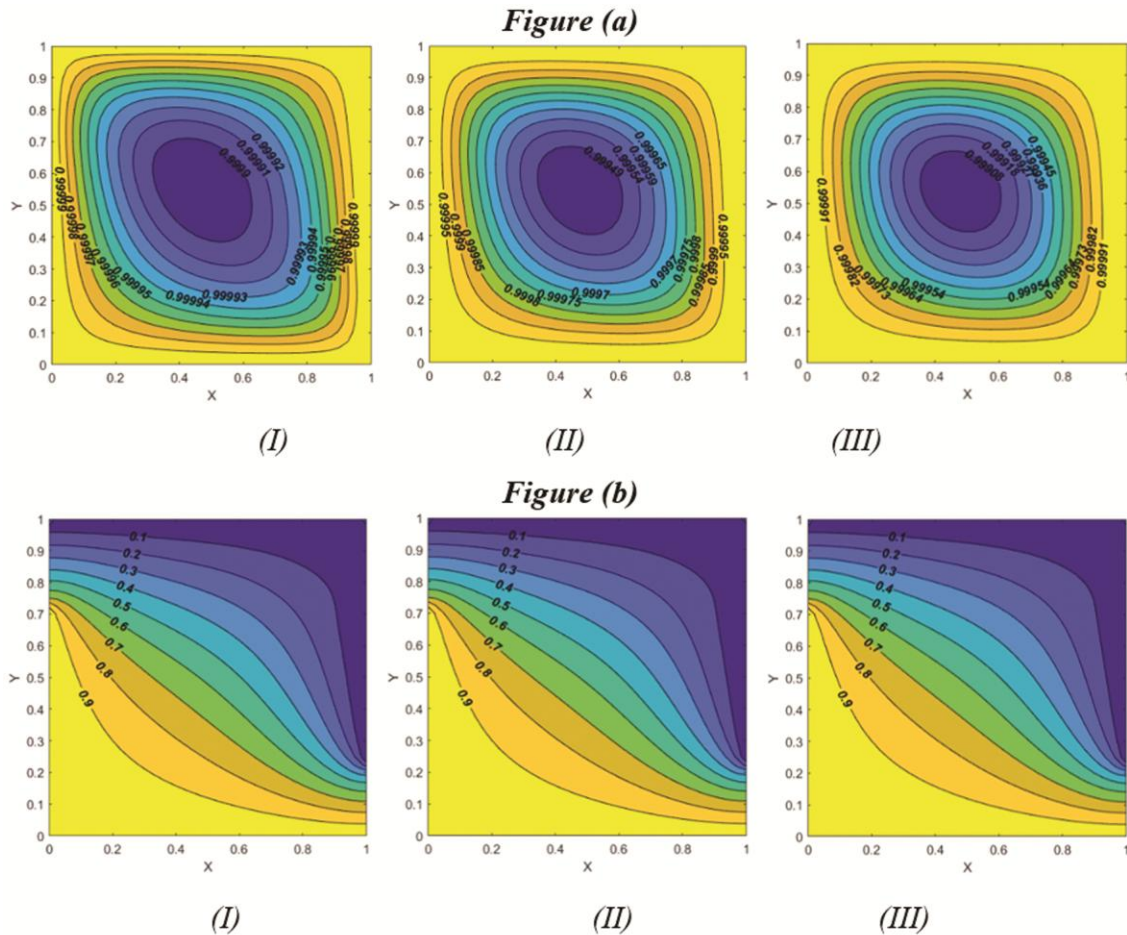


Fig. 3 — Streamlines (top) and isotherms (bottom) for fixed values of  $Re = 2, Ri = 1, Ha = 10, \gamma = 30^\circ, \gamma_e = 0.02$  varying (I)  $Da = 0.001$ , (II)  $Da = 0.01$  and (III)  $Da = 0.1$

#### Effects of the Darcy parameter

Fig. 3 depicts the various Darcy numbers effects on the streamlines. Increasing the Darcy number implies that the medium becomes more porous, the fluid permeability of the porous layer increases, and flow through the porous layer experiences little resistance. In some other way, by reducing the Darcy number, the flow through the porous layer experiences little resistance, as shown in Fig. 3a. The velocity is significantly affected by increasing the  $Da$  from 0.001 to 0.1. We noticed that the greater value of  $Da$ , the faster the streamlines flow in a clockwise direction. Fig. 3(b) depicts the isotherm effect at various Darcy numbers. Fluid velocity increases as the Darcy number increases, causing the square cavity temperature to rise. This is due to increasing the permeability  $Da$  of the medium, resulting in more free space for nanofluid recirculation and thus a higher velocity.

#### Effects of Hartmann Number

Fig. 4 illustrates three different Hartmann number effects on streamlines and isotherms in the case of mixed convection ( $Ri=1$ ). When the magnetic field  $Ha=10$  in Fig. 4a, the streamline occurs at the core regions of the cavity. Because the magnetic field strength increases to  $Ha = 25$  and  $Ha = 50$ , the circulation of the flow decreases, the fluid slows down, and the streamlines appear stretched, which indicate the decrease in fluid flow in the cavity when the magnetic field increases.

A magnetic field causes a Lorentz force to be generated in the opposite direction of flow. In Fig. 4b, the increase in the Hartmann number clearly shows that the changes in the isotherms are marginal. The hot profiles are created at the lower diagonal, whereas the cold profiles are generated at the upper diagonal of the isotherm contours. Hence the Hartmann number significantly affects the isotherms, with the same effect.

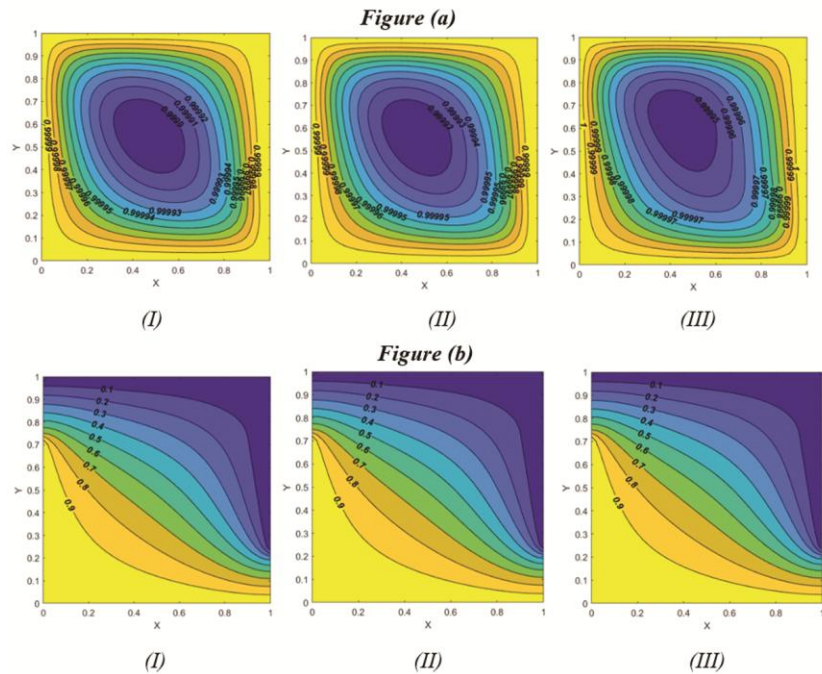


Fig. 4 — Streamlines(top) and isotherms(bottom) for fixed values of  $Re = 2, Ri = 1, Da = 0.001, \gamma = 30^\circ, \gamma_e = 0.02$  varying (I)  $Ha = 10$  (II)  $Ha = 25$  (III)  $Ha = 50$

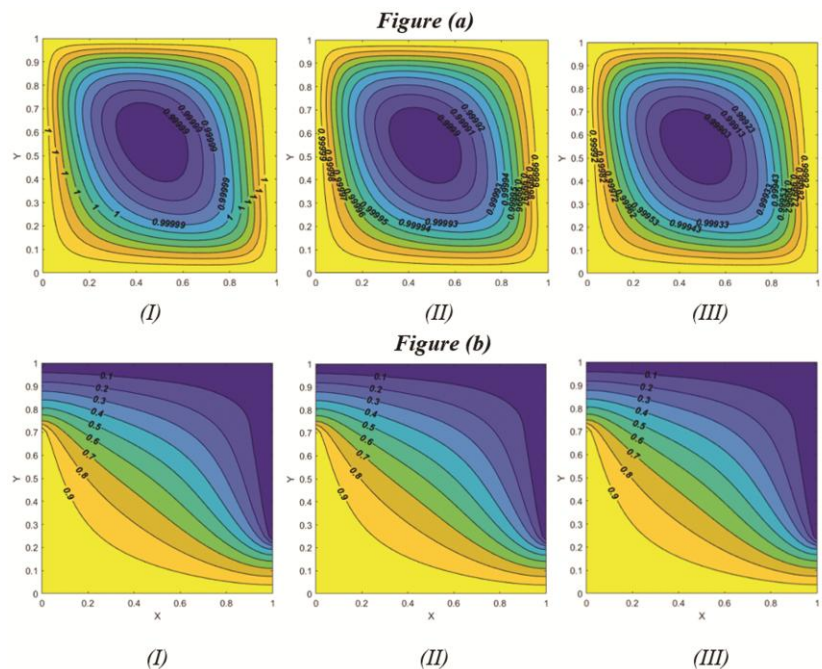


Fig. 5 — Streamlines(top) and isotherms(bottom) for fixed values of  $Re = 2, Ha = 10, Da = 0.001, \gamma = 30^\circ, \gamma_e = 0.02$  varying (I)  $Ri = 0.1$  (II)  $Ri = 1$  (III)  $Ri = 10$

#### Effects of Richardson Number

The operating flow regime is being researched by varying the values of the key dominating parameter, the Richardson number. For small  $Ri$  ( $Ri \leq 0.1$ ), forced convection takes precedence, and for  $Ri = 1$ ,

mixed convection dominates. On the other hand,  $Ri > 10$  corresponds to strong free convection. These variations, and the results for varying  $Ri$  (0.1, 1, and 100), are shown in Fig. 5 to visualize the combined effects of streamlines (top) and isotherms (bottom).

Fig. 5(a) shows how sensitive the streamline pattern is to changes in the Richardson number (Ri). From streamlined contours, there exists a cell that circulates clockwise in the centre which shows an increasing value from the centre. As the Ri values are raised for  $Ri=1$  and  $Ri=10$ , there will be noticeable changes in the lines as well as the values. According to isotherms, hot diagonal regions are generated at the lower diagonal and then cold regions at the upper diagonals.

**Effects of Magnetic field angle**

The impact of changing the gradient angle of the magnetic field on the flow of streamlines and isotherms is shown in Fig. 6 for three inclination angles ( $30^\circ, 45^\circ, 60^\circ$ ). For  $\gamma = 30^\circ$  the single circulation of streamlines (Fig. 6a) encountered almost throughout the entire cavity, while increasing the inclination,  $\gamma = 45^\circ$  there will be a noticeable change in contours, and the primary cell moves

towards the top left corner. As  $\gamma$  increases to  $60^\circ$  the circulation patterns are seen in the counter-clockwise direction. The dilatant fluid exhibits a stronger rotational effect while increasing the inclination. According to isotherms, however, they are mostly unaffected by a rise in the magnetic field inclination. But at the centre of the cavity, heat is transferred to the hot region, and the remaining region of the cavity is transferred by cold region.

**Effects of Reynolds number**

Fig. 7 shows the influence of the Reynolds number on streamlines and isotherms. When  $Re=2$ , the streamlines (Fig. 7a) of fluid flow occupy almost the entire domain and change to a circular shape, and the central region radiates cold. Raising the Reynolds number values for  $Re=5$  and  $Re=10$  the coefficient of heat transfer of fluid increases and enables the fluid flow to spread faster, which generates a hotter region with elongated streamlines. Fig. 7b shows the

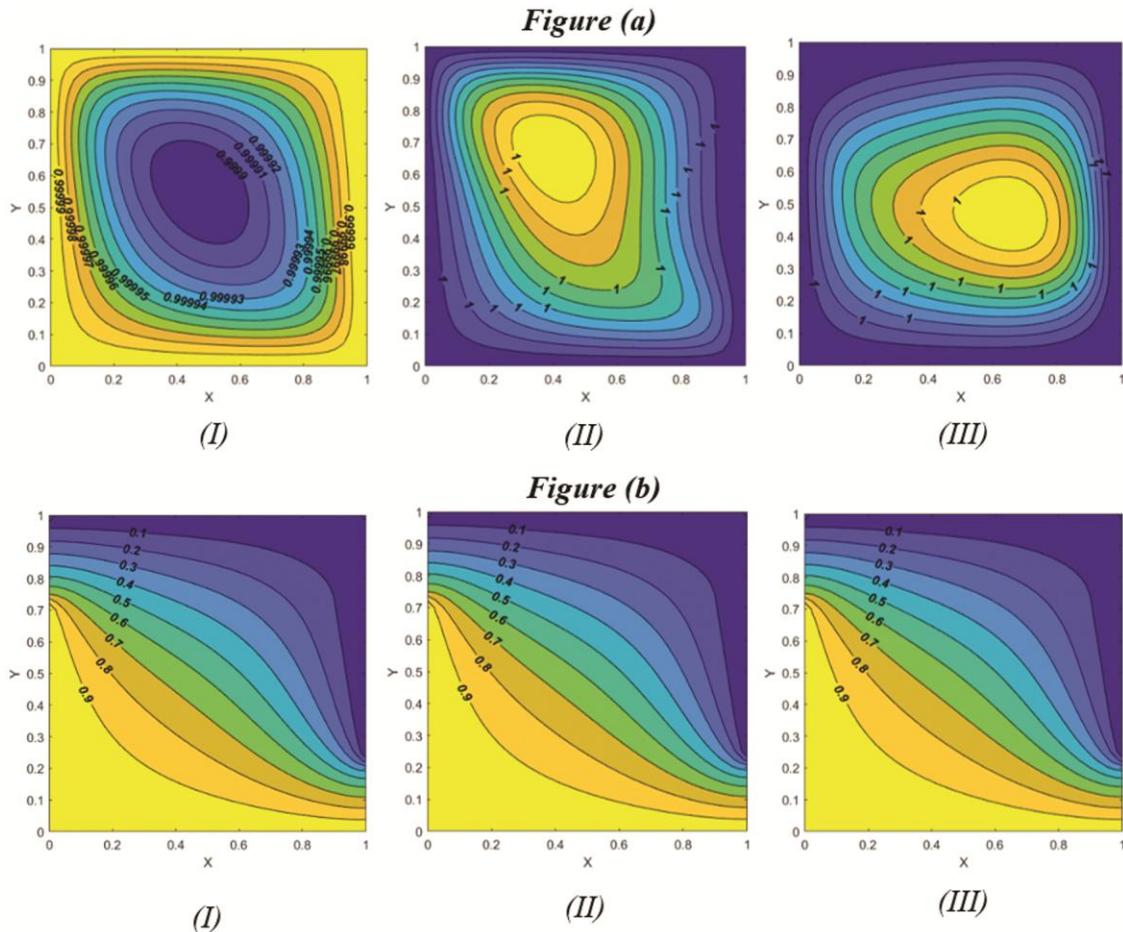


Fig. 6 — Streamlines(top) and isotherms(bottom) for fixed values of  $Re = 2, Ha = 10, Da = 0.001, Ri = 1, \gamma_e = 0.02$  varying (I)  $\gamma = 30^\circ$ , (II)  $\gamma = 45^\circ$  and (III)  $\gamma = 60^\circ$

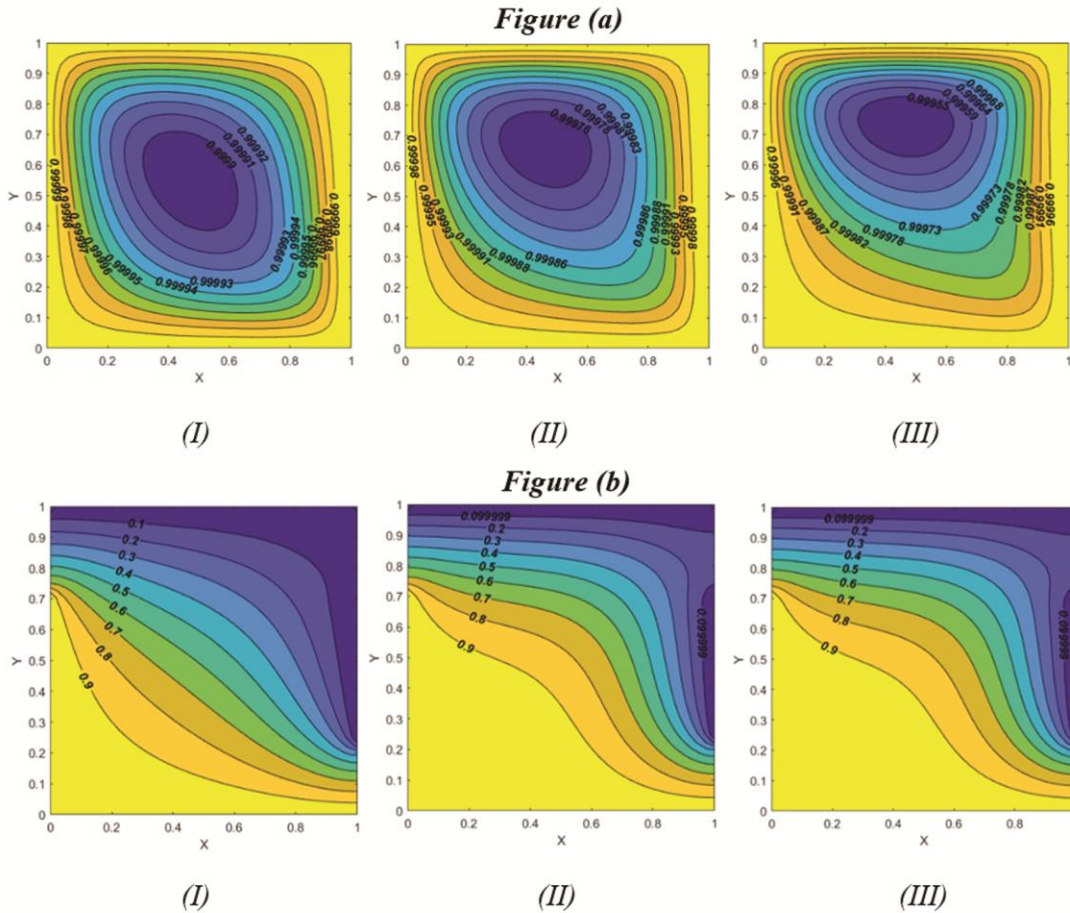


Fig. 7 — Streamlines(top) and isotherms(bottom) for fixed values of  $Ri = 1, Ha = 10, Da = 0.001, \gamma = 30^\circ, \gamma_e = 0.02$  varying (I)  $Re = 2$ , (II)  $Re = 5$  and (III)  $Re = 10$

corresponding isotherm plots. The figure clearly shows that the Reynolds number has a significant effect on isotherms at various convection regimes. When  $Re=2$ , the heat transformation took place in the lower diagonal, and when increasing the  $Re$  values ( $Re=5$  &  $10$ ) the heat transforms more efficiently towards the upper diagonal and the top right corner the cold eddies started spreading.

**Effects of Nusselt Number**

The characteristics of various parameters on local Nusselt profiles are shown in Fig. 8. For a variety of Darcy numbers. Fig. 8a depicts the local Nusselt number profiles along the heated wall in the square cavity filled with  $Al_2O_3/Cu - Oil$ . It can be seen that as the Darcy number rises, so do the local Nusselt numerical values. The impact of two different nanoparticle ( $Al_2O_3/Cu$ ) volume fractions at various levels is depicted in Fig. 8b. The high Nusselt number attains its maximum volume fraction level

furthermore it increases at the maximizing level. The local Nusselt number profiles are shown in Fig. 8c for the Richardson number for various values. As the Richardson number rises, so does the local Nusselt number. Also, by raising all  $Ri$  values, the Nusselt number also increases and they coincide as depicted in the figure.

**Results of Response Surface Methodology (RSM) and Optimization**

The RSM is among the most useful tools for examining the effects of multiple variables and factors when they have an impact on the response variable. The RSM is an effective testing design for analysing the concurrent effects of multiple variables because it requires the least amount of resources and quantitative data. An empirical relationship between the response variables can be developed using the RSM. The characteristics of the response variables are predicted and optimized using this empirical relationship.

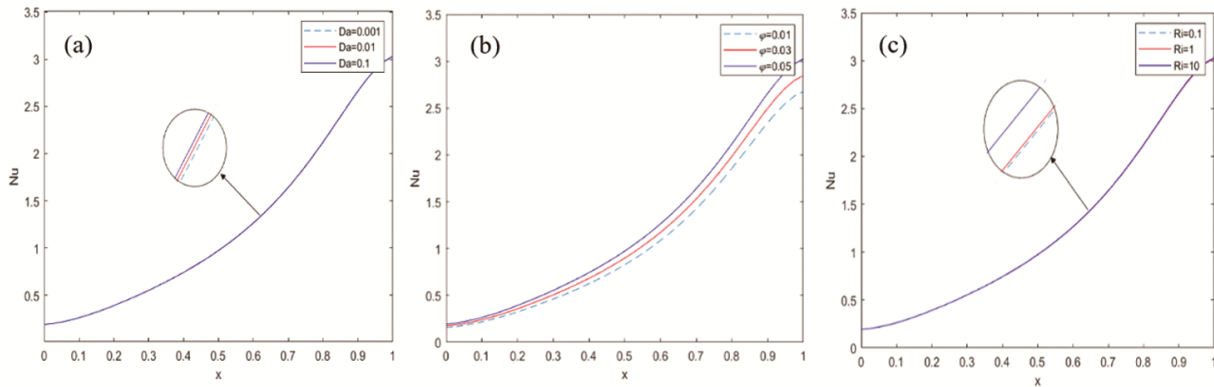


Fig. 8 — The local Nusselt profiles for different parameters: (a) Darcy number( $Da$ ) (b)Volume fraction ( $\varphi$ ) and (c) Richardson number ( $Ri$ )

Table 3 — The RSM key parameters, their symbols, and their levels

Key factors	Symbols	Levels		
		-1 (Low)	0 (Medium)	1 (High)
Da	$X_1$	0.001	0.01	0.1
$\varphi$	$X_2$	0.01	0.03	0.05
Ha	$X_3$	10	25	50

Table 4 — Heat transfer rate ( $Nu_{Avg}$ ) experimental design and responses

Order	Coded Values			Real Values			AvNu
	$X_1$	$X_2$	$X_3$	Da	$\varphi$	Ha	
1	-1	-1	-1	0.001	0.01	10	1.06653298763627
2	1	-1	-1	0.1	0.01	10	1.06838692005102
3	-1	1	-1	0.001	0.05	10	1.23035096290127
4	1	1	-1	0.1	0.05	10	1.23208057555806
5	-1	-1	1	0.001	0.01	50	1.06639347881466
6	1	-1	1	0.1	0.01	50	1.06648600324029
7	-1	1	1	0.001	0.05	50	1.06639347881466
8	1	1	1	0.1	0.05	50	1.23030664482191
9	-1	0	0	0.001	0.03	25	1.14641987509095
10	1	0	0	0.1	0.03	25	1.14689986253511
11	0	-1	0	0.01	0.01	25	1.14677967526593
12	0	1	0	0.01	0.05	25	1.23065027247192
13	0	0	-1	0.01	0.03	10	1.14742599938471
14	0	0	1	0.01	0.03	50	1.14641041611618
15	0	0	0	0.01	0.03	25	1.14677967526593
16	0	0	0	0.01	0.03	25	1.14677967526593
17	0	0	0	0.01	0.03	25	1.14677967526593
18	0	0	0	0.01	0.03	25	1.14677967526593
19	0	0	0	0.01	0.03	25	1.14677967526593
20	0	0	0	0.01	0.03	25	1.14677967526593

Additionally, by examining the interactive effects of key parameters on the response variable, the key parameters can be set to optimal values. Additional details provide more information on this technique<sup>49-52</sup>.

**Test methodology**

The response surface method helps to obtain the optimal state of the parameters that have the greatest impact on the findings. The ongoing RSM model looks

into the combined effects of Darcy number ( $0.001 \leq Da \leq 0.1$ ), nanoparticle volume fraction ( $0.01 \leq \varphi \leq 0.05$ ) and Hartmann number ( $10 \leq Ha \leq 50$ ) on  $Al_2O_3 - Cu - Oil$  hybrid nanofluid inside the square cavity. The different combinations are used to build a statistical table. The Darcy number ( $Da$ ), nanoparticle volume fraction ( $\varphi$ ), and Hartmann number ( $Ha$ ) parameters are combined to create a statistical table. To find the best values for these variables in order to

Table 5 — ANOVA for Quadratic model of ( $Nu_{Avg}$ )

Source	Deg. of Freedom	Adj. Sum of Squares	Adj. Mean Square	F Value	P Value
Model	9	0.052446	0.005827	7.69	0.002
Linear	3	0.040084	0.013361	17.63	0.000
Da	1	0.003072	0.003072	4.05	0.072
$\phi$	1	0.034940	0.034940	46.09	0.000
Ha	1	0.002028	0.002028	2.68	0.133
Square	3	0.005214	0.001738	2.29	0.140
Da*Da	1	0.002758	0.002758	3.64	0.086
$\phi * \phi$	1	0.000978	0.000978	1.29	0.282
Ha*Ha	1	0.000714	0.000714	0.94	0.355
2-way interaction	3	0.009248	0.003083	4.07	0.040
Da* $\phi$	1	0.004219	0.004219	5.57	0.040
Da*Ha	1	0.002028	0.002028	2.68	0.133
$\phi * Ha$	1	0.003274	0.003274	4.32	0.064
Error	10	0.007581	0.000758		
Lack-of-Fit	5	0.007581	0.001516	*	*
Pure Error	5	0.000000	0.000000		
Total	19	0.060027			

$R^2=99.98\%$

maximize heat transfer rate, consider the three previously mentioned essential components at the following levels: low (1), medium (0), and high (+1). The primary elements, their codes, and their levels are listed in Table 3. According to the formula  $2^k + 2k + F$ , this design has 20 runs, as shown in Table 4.

#### Accuracy of the model

The accuracy of the RSM model is evaluated using the following ANOVA table. When the value of p is less than 0.05 (taking into account the 95% level of significance), a parameter is generally considered statistically significant. The statistical significance is established when the p-value for the model is less than 0.05, as shown in Table 5, which accounts for the 95% level of significance.

The linear term Ha, the square terms  $\phi * \phi$  and  $Ha * Ha$  also the interaction term Da\*Ha are negligible in the framework due to their insignificance. The accuracy of the model for the selected range of parameters is supported by the fact that the determination coefficients for both models are also high (99.98% and 99.97%, respectively). It is also used to evaluate how accurate the models are. The model is a perfect match because of the strong fit  $R^2=99.98\%$ .

The accuracy of the model can be evaluated using the residual plots (Fig. 9). The histogram bell-shaped appearance and the fact that the data points are arranged in a straight line indicate that the residuals follow a normal distribution. The residual-versus-fitted plot demonstrates that the largest deviation of

the model is nearly 0.015. These plots show how accurate the model is for the given parameter range.

#### Statistical interpretations

Regarding the un-coded parameters (Da, and Ha), the quadratic functional form of the regression coefficient for Table 6 is as follows:

$$Nu_{avg} = 1.0537 + 3.55 Da + 0.58 \phi + 0.00263 Ha - 42.6 Da * Da + 47.2 \phi * \phi - 0.000043 Ha * Ha + 21.80 Da * \phi + 0.01501 Da * Ha - 0.0503 \phi * Ha \dots (40)$$

The outcomes of this functional application of the typical Nusselt number are as follows. According to the regression coefficient results (Table 6), Da,  $\phi$  and Ha are positively correlated, indicating that raising these parameters causes a decline in  $Nu_{avg}$ .

The interaction between Da,  $\phi$  and Ha on mean heat transfer rate  $Nu_{avg}$  is shown in Fig. 10. The influence of the other two parameters is examined in contours and surface plots by holding the third parameter constant (at the medium level). Fig. 10a depicts the outcome of Da when Ha is frozen. The upper left corner has the highest heat transfer coefficient when Da is maximum and Da is minimum. Fig. 10b illustrates how  $\phi$  and Ha interact when Da is frozen. When Ha is at its maximum and Da is at its lowest, the right corner experiences the greatest heat transfer. The interaction effect of Ha and Da when  $\phi$  is frozen is shown in Fig. 10c. The greatest heat transfer occurs at the middle values of Da and Ha.

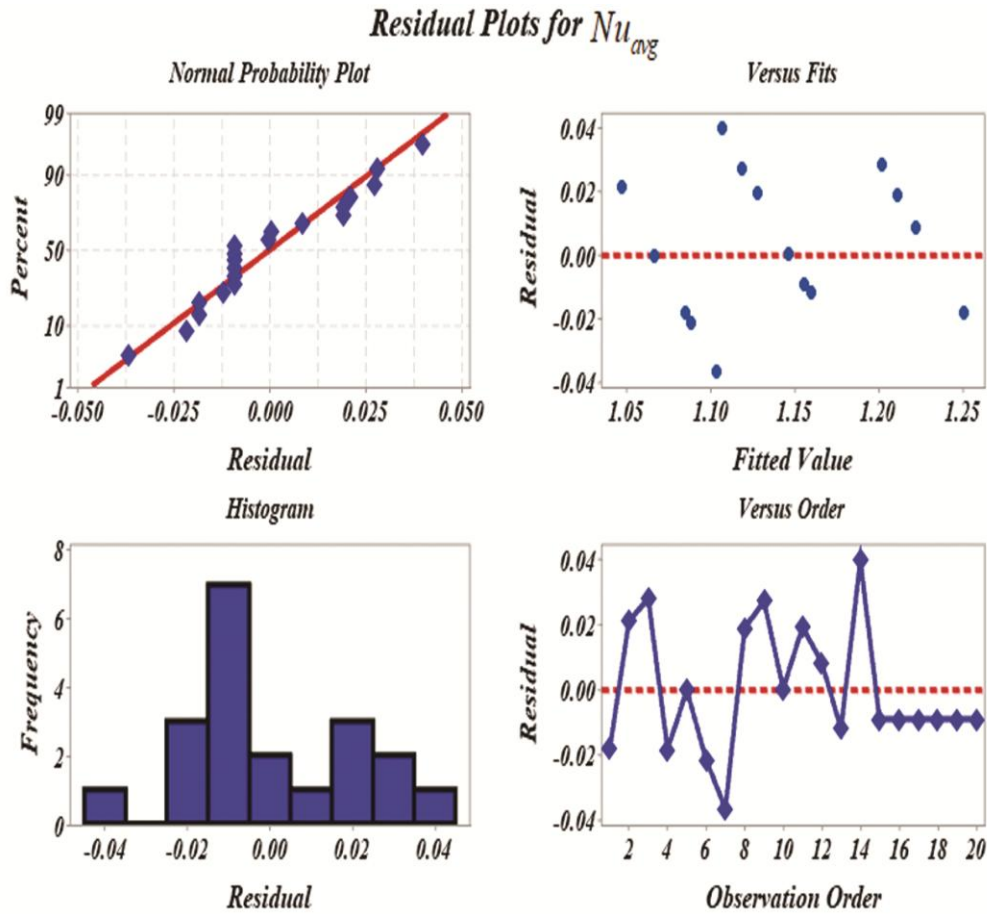


Fig. 9 — Residual plots for  $Nu_{avg}$

Table 6 — Sensitivity values for all critical factor levels

Order	$X_1$	$X_2$	$X_3$	$\frac{\partial Nu_{avg}}{\partial X_1}$	$\frac{\partial Nu_{avg}}{\partial X_2}$	$\frac{\partial Nu_{avg}}{\partial X_3}$
1	0	-1	-1	3.06610	1.2390	0.0031371
2	0	-1	0	3.29125	0.4845	0.0044271
3	0	-1	1	3.66650	-0.7730	0.0065771
4	0	0	-1	3.50210	3.1270	0.0021311
5	0	0	0	3.72725	2.3725	0.0034211
6	0	0	1	4.10250	1.1150	0.0055711
7	0	1	-1	3.93810	5.0150	0.0011251
8	0	1	0	4.16325	4.2605	0.0024151
9	0	1	1	4.53850	3.0030	0.0045651

**Sensitivity analysis**

In this section, the sensitivity of the heat transmission rate is estimated. The evolution of the response variable as the pertinent parameters are increased is described in detail by the sensitivity analysis. The derivative of the average heat transfer coefficient from the input parameters is calculated in order to examine how sensitive the mean heat transfer coefficient ( $Nu_{avg}$ ) is to the input parameters  $Da$ ,  $\varphi$

and  $Ha$ . A positive correlation implies a positive sensitivity. The quadratic model is partially differentiated with respect to the required task in order to obtain the sensitivity function. The derived form of Eq. (40) for the input parameters is as follows:

$$\frac{\partial Nu_{avg}}{\partial Da} = 3.550 - 85.20X_1 + 21.80X_2 + 0.01501X_3, \dots \quad (41)$$

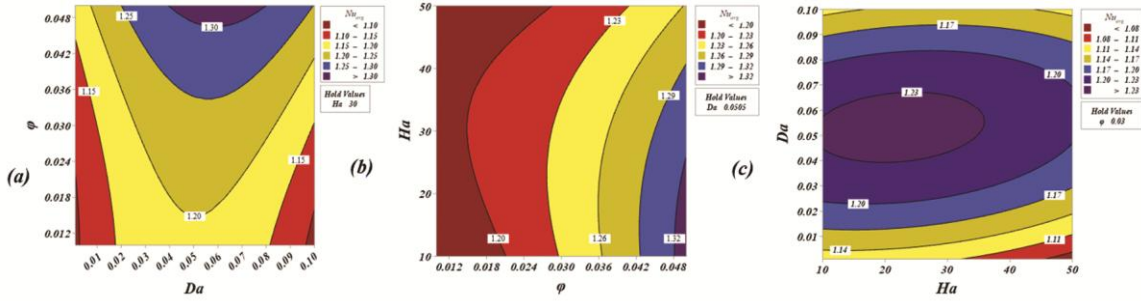


Fig. 10 — (a)-(c)Response surface and contour plots ( $Nu_{avg}$ )with respect to the  $Da$ ,  $\phi$  and  $Ha$ , respectively

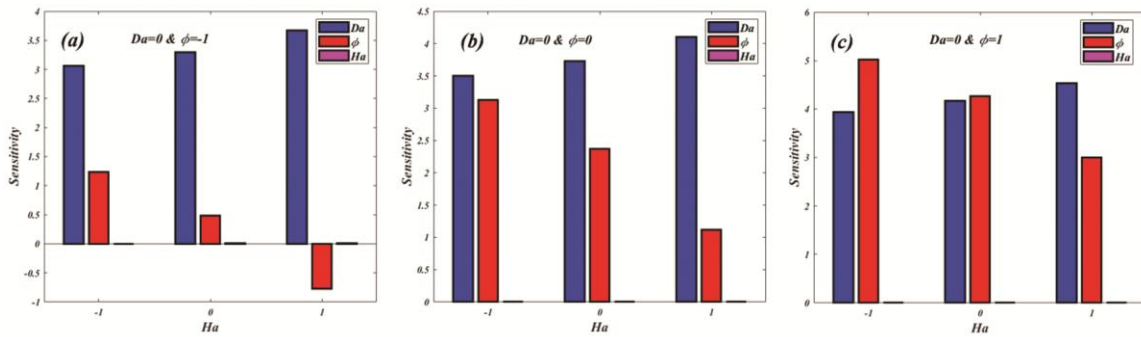


Fig. 11 — Sensitivity of  $Nu_{avg}$

$$\frac{\partial Nu_{avg}}{\partial \phi} = 0.58 + 21.80X_1 + 94.40X_2 - 0.0503X_3, \dots \quad (42)$$

$$\frac{\partial Nu_{avg}}{\partial Ha} = 0.00263 + 0.01501X_1 - 0.0503X_2 + 0.000086X_3, \dots \quad (43)$$

The afore mentioned Eqs. (41-43) relate the input parameters to the mean heat transfer rate. When the objective function increases as the input parameters increase, a positive sensitivity value is obtained.

Table 6 summarizes the result of the  $Nu_{avg}$  sensitivity values for the important components at all levels. It can be seen that the sensitivities of all parameters are positive. To say it another way, the increase in these parameters resulted in an improvement in ( $Nu_{avg}$ ).

The sensitivity of the response to the variable increases with increasing the bar graph height. The positive sensitivity will result, and vice versa, if an increase in one variable causes an increase in the other. Using bar charts, Fig. 11 illustrates the sensitivity of the mean heat transfer rate. The sensitivity values offer details for correlating the effects of a parameter increment. In order to conclude, the sensitivity of the response to the variable increases with increasing bar graph height. As can be seen in

Fig. 11, ( $Nu_{avg}$ ) is most enhanced by the change in  $\phi$ . (highest sensitivity).The responses have decreased and improved as shown by the negative and positive bar charts. Fig.11a demonstrates that the mean Nusselt number sensitivity changes to the positive Darcy parameter ( $Da=0.01$ ) is present with a volume fraction ( $\phi =0.01$ ) other than there is a reduction in volume fraction when for  $Ha$  ranging from 10 to 50. Fig.11b demonstrates that the sensitivity of mean Nusselt number decreases for  $Ha$  values between 10 and 50 when the Darcy parameter ( $Da=0.01$ ) and the volume fraction ( $\phi$ ) are both set to 3%.The sensitivity of mean Nusselt number to changes in  $Ha$  is shown in Fig. 11c when the volume fraction ( $\phi=0.05$ ) and Darcy parameter ( $Da=0.01$ ) are frozen at their midpoint values. The sensitivities to B and C lead to an increase in ( $Nu_{avg}$ ).

The following outcomes arise from increasing the key factor levels:

- The maximum heat transfer rate obtained from the statistical experiment is 1.3322 by fixing  $Ha=11.2121$ ,  $Da=0.0560$  and  $\phi =0.05$ .
- The minimum heat transfer rate obtained from the statistical experiment is 1.0472 by fixing  $Ha=10$ ,  $Da=0.10$  and  $\phi =0.01$ .

## Conclusion

The  $Al_2O_3/Cu - Oil$  hybrid nanofluid is investigated for its effects in the presence of, mixed convection inside a square cavity with complex boundary conditions. The governing equations are reduced to dimensionless form before being numerically resolved using the finite difference MAC technique. The current study seeks to address the framework with the heat flux model Cattaneo-Christov in a lid-driven, porous cavity. Several parameters like Richardson number (Ri), Reynolds number (Re), nanoparticle volume fraction ( $\phi$ ), and magnetic field angle ( $\gamma$ ) are discussed through streamlines, isotherms, and average and local Nusselt numbers. The following are the most important observations are summarized:

- ❖ Increasing the Darcy number (Da) value implies an increase in the fluid permeability.

- ❖ It is noticed that when the magnetic field (Ha) strengthens, the fluid flow decreases due to decrease in thermal conductivity.

- ❖ If the Richardson number  $Ri \leq 1$ , buoyancy has no effect on the flow. If  $Ri \geq 1$ , buoyancy takes precedence (in the sense that the kinetic energy there is insufficient to homogenize the fluids).

- ❖ If the Richardson number  $Ri = 1$ , the flow is almost certainly buoyancy-driven: the energy of the flow is derived from the potential energy in the system.

- ❖ As the Reynolds number (Re) increases, so does the heat conductivity and thus the fluid flow in the system.

- ❖ According to the current model, the  $Al_2O_3/Cu - Oil$  nanofluid has higher heat transfer.

- ❖ When the Hartmann number is increased, the average Nusselt number decreases.

## References

- 1 Das S K, Choi S U S & Patel H E, *Heat Transf Eng*, 27 (2006) 3.
- 2 Eastman J A, Choi U S, Li S, Thompson L J & Lee S, *Mater Res Soc Symp Proc*, 457 (1997) 3.
- 3 Choi S U S, Zhang Z G, Yu W, Lockwood F E & Grulke E A, *Appl Phys Lett*, 79 (2001) 2252.
- 4 Eastman J A, Choi S U S, Li S, Yu W & Thompson L J, *Appl Phys Lett*, 78 (2001) 718.
- 5 Yu W, France D M, Routbort J L & Choi S U S, *Heat Transf Eng*, 29 (2008) 432.
- 6 Asadi A, Alarifi I M & Foong L K, *J Mol Liq*, 307 (2020) 112987.
- 7 Abu-Nab A K & Abu-Bakr A F, *Case Stud Therm Eng*, 33 (2022) 101973.
- 8 Khashi'ie N S, Arifin N M & Pop I, *Chinese J Phys*, 78 (2022) 169.
- 9 Alsabery A I, Tayebi T, Ghalambaz H T M, Hashim I & Chamkha A J, *J Adv Res*, 30 (2021) 63.
- 10 Zhang Y, Shahmir N, Ramzan M, Alotaibi H & Aljohani H M, *Case Stud Therm Eng*, 26 (2021) 101149.
- 11 Khan M J, Duraiswamy B, Zuhra S, Nawaz R, Nisar K S, Jamshed W & Yahia I S, *Case Stud Therm Eng*, 28 (2021) 101673.
- 12 Haddad S A M, *Int J Heat Mass Transf*, 68 (2014) 659.
- 13 Minea A A, *Int J Heat Mass Transf*, 104 (2017) 852.
- 14 Usman M, Hamid M, Zubair T, Haq R U & Wang W, *Int J Heat Mass Transf*, 126 (2018) 1347.
- 15 Siddiqui F R, Tso C Y, Chan C K, Fu S C & Chao C Y H, *Int J Heat Mass Transf*, 132 (2019) 1200.
- 16 Aghakhani S, Pordanjani A H, Afrand M, Sharifpur M & Meyer J P, *Int J Mech Sci*, 174 (2020) 105470.
- 17 Moghadassi A, Ghomi E & Parviziyan F, *Int J Therm Sci*, 92 (2015) 50.
- 18 Das S, Sarkar S & Jana R N, *Bionanoscience*, 10 (2020) 950.
- 19 Kadhim H T, Jabbar F A & Rona A, *Int J Mech Sci*, 186 (2020) 105889.
- 20 Sui J, Zheng L & Zhang X, *Int J Therm Sci*, 104 (2016) 461.
- 21 Reddy M G, Rani S M V V N L, Kumar K G, Prasannakumar B C & Lokesh H J, *Phys A Stat Mech Appl*, 551 (2020) 123975.
- 22 Garia R, Rawat S K, Kumar M & Yaseen M, *Chinese J Phys*, 74 (2021) 421.
- 23 Elshehaby H M, Hady F M, Ahmed S E & Mohamed R A, *Int Commun Heat Mass Transf*, 57 (2014) 228.
- 24 Du R, Gokulavani P, Muthamilselvan M, Al-Amri F & Abdalla B, *Int Commun Heat Mass Transf*, 116 (2020) 104676.
- 25 Mehryan S A M, Kashkooli F M, Ghalambaz M & Chamkha A J, *Adv Powder Technol*, 28 (2017) 2295.
- 26 Suresh S, Venkataraj K P, Selvakumar P & Chandrasekar M, *Colloids Surfaces A Physicochem Eng Asp*, 388 (2011) 41.
- 27 Aladdin N A L, Bachok N & Pop I, *Alex Eng J*, 59 (2020) 657.
- 28 Tahira S, Mustafa M & Mushtaq A, *Proc Inst Mech Eng Part C J Mech Eng Sci*, 236 (2022) 1524.
- 29 Lund L A, Omar Z, Khan I, Seikh A H, Sherif E S M & Nisar K S, *J Mater Res Technol*, 9 (2020) 421.
- 30 Abu-Hamdeh N H, Abusorrah M A, Bayoumi M M, Oztop H F & Sun C, *J Therm Anal Calorim*, 144 (2021) 2627.
- 31 Khan J A, Mustafa M, Hayat T & Alsaedi A, *PLoS One*, 10 (2015) 1.
- 32 Christov C I, *Mech Res Commun*, 36 (2009) 481.
- 33 Devi S S U & Devi S P A, *Can J Phys*, 94 (2016) 490.
- 34 Meena O P & Pranitha J, *AIP Conf Proc*, 2246 (2020) 020019.
- 35 Pranitha J & Meena O P, *Int J Eng Sci*, 2 (2020) 9.
- 36 Meena O P, Pranitha J & Ganesh K K, *Appl Math Comput*, 430 (2022) 127072.
- 37 Meena O P, Pranitha J & Srinivasacharya D, *Int J Appl Comput Math*, 7 (2021) 59.
- 38 Khan H B M D, Prasad V R & Bhuvana V R, *Nonlinear Eng*, 7 (2018) 253.
- 39 Venkatadri K, Bég O A, Rajarajeswari P & Prasad V R, *Int J Mech Sci*, 171 (2020) 105391.

- 40 Bég O A, Venkatadri K, Prasad V R, Bég T A, Kadir A & Leonard H J, *Mater Sci Eng B Solid State Mater Adv Technol*, 261 (2020) 114722.
- 41 Pordanjani A H, Vahedi S M, Aghakhani S, Afrand M, Öztop H F & Abu-Hamdeh N, *Eur Phy J Plus*, 134 (2019) 12763.
- 42 Hayat T, Muhammad T, Alsaedi A & Mustafa M, *PLoS One*, 11 (2016) 1.
- 43 Alnaqi A A, Aghakhani S, Pordanjani A H, Bakhtiari R, Asadi A & Tran M D, *Int J Heat Mass Transf*, 133 (2019) 256.
- 44 Kashyap D & Dass A K, *Int J Mech Sci*, 157 (2019) 45.
- 45 Mehryan S A M, Izadpanahi E, Ghalambaz M & Chamkha A J, *J Ther Anal Calorim*, 137 (2019) 965.
- 46 Brinkman H C, *J Chem Phys*, 20 (1952) 571.
- 47 Pirmohammadi M & Ghassemi M, *Int Commun Heat Mass Transf*, 36 (2009) 776.
- 48 Sarris I E, G K Zikos, Grecos A P & Vlachos N S, *Numer Heat Transf B: Fundament: An Int J*, 50 (2007) 157.
- 49 Rashad A M, Chamkha A J, Ismael M A & Salah T, *J Heat Transfer*, 140 (2018) 7.
- 50 Mamourian M, Shirvan K M & Pop I, *Int Commun Heat Mass Transf*, 79 (2016) 46.
- 51 Shirvan K M, Mamourian M, Mirzakhanlari S, Ellahi R & Vafai K, *Int J Heat Mass Transf*, 105 (2017) 811.
- 52 Mackolil J & Mahanthesh B, *Appl Nanosci*, (2021) 01631. DOI:10.1007/s13204-020-01631-4